JGR Oceans

RESEARCH ARTICLE
10.1029/2025JC022632

Weakened Stratification Across the Eurasian Basin Enables Enhanced Vertical Spreading of Atlantic Water

F. Challet[1], C. Herbaut[1], M.-N. Houssais[1], and G. Meneghello[2]

[1]LOCEAN, Sorbonne Université, CNRS, IRD, MNHN, Paris, France, [2]LMD, Ecole Normale Supérieure, Paris, France

Key Points:

- The hydrographic variability of the Eurasian Basin is marked by long-term trends as well as warm and saline anomalies
- Both anomalies and trends are concentrated in the thermocline and accompanied by weakened stratification in the Atlantic Water
- Model results show how stratification-driven changes in vertical diffusion could accumulate heat and salt in the thermocline

Supporting Information:

Supporting Information may be found in the online version of this article.

Correspondence to:

F. Challet,
francois.challet@locean.ipsl.fr

Citation:

Challet, F., Herbaut, C., Houssais, M.-N., & Meneghello, G. (2025). Weakened stratification across the Eurasian Basin enables enhanced vertical spreading of Atlantic Water. *Journal of Geophysical Research: Oceans*, *130*, e2025JC022632. https://doi.org/10.1029/2025JC022632

Received 12 MAR 2025
Accepted 23 OCT 2025

Author Contributions:

Conceptualization: F. Challet, C. Herbaut, M.-N. Houssais, G. Meneghello
Data curation: F. Challet
Investigation: F. Challet, C. Herbaut, M.-N. Houssais, G. Meneghello
Methodology: F. Challet, C. Herbaut, M.-N. Houssais, G. Meneghello
Software: F. Challet
Supervision: C. Herbaut, M.-N. Houssais, G. Meneghello
Validation: F. Challet, C. Herbaut, M.-N. Houssais, G. Meneghello
Visualization: F. Challet
Writing – original draft: F. Challet
Writing – review & editing: C. Herbaut, M.-N. Houssais, G. Meneghello

Abstract

Ocean stratification plays a crucial role in regulating heat fluxes from the ocean to the sea ice and atmosphere. In the Arctic Ocean, a layer of fresh and cold Polar Water near the surface isolates warm and saline Atlantic Water (AW) due to a strong halocline. While the stratification in the eastern Eurasian Basin halocline is known to have weakened since the 2000s, we here investigate the variability of stratification over the full AW depth range at basin scale. We analyze 40 years of in situ hydrographic data to track changes in stratification across the entire Eurasian Basin and introduce a conceptual dynamical model to explain the underlying mechanisms. Our results show that the most pronounced temperature and salinity variability occurs in the ~100 m thick thermocline, which separates warm AW at depth from the colder, fresher halocline above. This variability is driven by warm, saline anomalies lasting for a few years entering through Fram Strait and propagating along the boundary current, superimposed on long-term trends. Our combined observational and modeling approach reveals that thermocline stratification has weakened by up to 50% in many regions, enhancing the potential for upward diffusive fluxes of heat and salt toward the base of the halocline.

Plain Language Summary

Ocean stratification plays a key role in determining the response of the Arctic Ocean to climate change. Earlier studies have shown that the halocline, which protects sea ice from warmer water underneath, has become less stable in the eastern Eurasian Basin since the 2000s. The full range of changes down to the deeper, warmer, and saltier Atlantic Water (AW) layer has, however, been little studied. In this study, data from the past 35 years is analyzed to track stratification changes. We find that the temperature and salinity have varied the most in the so-called thermocline, which separates the warmer AW below from the colder, fresher halocline above. The changes in stratification are driven by both short-term anomalies of warm, saline water entering through Fram Strait and by a long-term warming and salinity increase. In many parts of the Eurasian Basin, the thermocline has become up to 50% less stable, making it easier for heat and salt to move upwards to the base of the halocline. Using a conceptual model, we propose a mechanism linking temperature and salinity changes to the stratification of the water column.

1. Introduction

Over the past four decades, the Arctic Ocean has undergone profound changes in response to anthropogenic climate change. The sea-ice cover has decreased significantly, associated with rising atmospheric surface temperatures (Rantanen et al., 2022) and ocean surface warming. Several studies point toward an increasing role of heat stored in the ocean subsurface on sea-ice retreat (Polyakov et al., 2004, 2017). Most of the oceanic heat input into the Arctic Ocean subsurface is supplied by the warm (>2°C) and relatively saline Atlantic Water (AW) entering the Arctic Ocean via Fram Strait and the Barents Sea, which then circulates around the Eurasian, Makarov and Canada Basins following the bathymetry (Figure 1a). Observations at Fram Strait show a heat content increase in these waters, which manifested both as a long-term trend and as intermittent short-term anomalies. A warming trend of 0.6°C/decade was found by Beszczynska-Möller et al. (2012) between 1997 and 2010 in the temperature of the AW at Fram Strait. Warm anomalies lasting for 2–3 years have also been observed. The first reported warm anomaly was observed in 1990 north of Franz Joseph Land and Severnaya Zemlya (Quadfasel et al., 1991) but could not be traced back to Fram Strait. A second warm anomaly was identified at Fram Strait in 1999 (Schauer et al., 2004); and observed to propagate toward the eastern Eurasian Basin, which was reached in 2004 (Polyakov et al., 2005). The best-documented anomaly entered Fram Strait in 2006–2007 (Beszczynska-Möller et al., 2012) and was estimated to reach the eastern Eurasian Basin 2 years later (Polyakov et al., 2020), but no study documented its presence further than in the Makarov Basin or along the Lomonosov Ridge in the current heading back toward Fram Strait. This event was followed by another warm anomaly entering Fram Strait in 2014–2016 (Challet et al., 2022). After 2017, a general cooling and freshening was observed in Fram Strait (Polyakov et al., 2023). This fresh anomaly was presumably associated with the arrival of a substantial fresh anomaly documented in the subpolar North Atlantic from the mid 2000s (Holliday et al., 2015).

In most of the central Arctic Ocean, the impact of increasing heat content in the AW on the evolution of sea ice has presumably been limited by the presence of the cold halocline layer (CHL), which separates the cold and fresh surface layer from the warm and saline AW layer underneath. Just below the CHL, in the thermocline, temperature increases rapidly with depth, accompanied by a more gradual increase in salinity, before reaching the warm, saline AW core which is characterized by a temperature maximum (Figure 1b). While the AW layer contains sufficient heat to melt the entire sea-ice cover of the Arctic Ocean several times over, the strong CHL's density stratification limits the heat flux between the AW and the surface layer to less than 1–2 W/m^2 across most of the Arctic Ocean (Carmack et al., 2015). However, evidence of a weakening of the CHL stratification was found in the eastern Eurasian Basin, close to the Laptev Sea (Polyakov et al., 2017), which could accelerate the pace of future sea-ice loss (Muilwijk et al., 2023). This contrasts with the Amerasian Basin where a strengthening of the halocline has been observed over the past decades (Morison et al., 2012; Rosenblum et al., 2022).

While the CHL certainly plays a central role in regulating heat fluxes between the warm AW and the surface, these fluxes are also likely influenced by hydrographic changes within the AW layer itself. At basin scale, observational studies of long-term hydrographic changes in the AW layer have primarily focused on the evolution of the AW core temperature (Richards et al., 2022), highlighting a warming from the 1990s to the 2000s (Polyakov et al., 2012), rather than on changes in the vertical distribution of the heat content. However, mooring data from the eastern Eurasian Basin show that hydrographic changes there have been dominated by a significant shoaling trend of the upper boundary of the AW layer since the early 2000s, leading to a larger ocean heat flux to the sea ice in winter in some places (Polyakov et al., 2017). The amplitude of this AW shoaling at basin scale and its physical drivers—in particular the role of AW properties and stratification changes, have, to our knowledge, been little investigated. In this study, we show evidence of a thickening trend of the AW layer across the entire Eurasian Basin, which is associated with upward and downward shifts of the upper and lower boundaries of the layer, respectively. We propose a mechanism to link this thickening trend to changes in the properties of the AW inflow entering the basin through Fram Strait.

Our analysis is organized as follows. We first map regional changes in the properties of the Arctic Ocean above the AW core for the entire Eurasian Basin based on observations. We then differentiate five subregions which are identified by coherent stratification characteristics (Section 2). The hydrographic development is shown separately for all five regions. We show that variability in both temperature and salinity is concentrated in the AW thermocline below the CHL, and that this variability is associated with reduced stratification in the thermocline down to the AW core (Section 3). Finally, we try to explain how temperature and salinity anomalies entering via Fram Strait have the potential to modify the stratification and vertical T-S distributions as they travel around the Eurasian basin, with the help of a simple advection-diffusion model able to reproduce conditions consistent with the observations (Sections 4 and 5).

2. Data and Methods

In the Arctic Ocean continuous time series are rarely available and most of the data are scattered in space. It is therefore challenging to create a consistent picture of trends and variability across large regions such as the Eurasian Basin (Richards et al., 2022). We propose a new method to divide the Eurasian Basin into several regions with coherent hydrographic properties and reconstruct separate time series of temperature, salinity, and stratification for the different regions, respectively. This approach provides an overview of the evolution of the hydrographic properties and the thickening of AW across the Eurasian Basin.

2.1. Data

Our data set consists of hydrographic data from the World Ocean Database (WOD, https://www.ncei.noaa.gov/products/world-ocean-data-base; Boyer et al., 2018) dating back to the 1980s, which are complemented with data from the MOSAIC expedition (Rabe et al., 2022; Tippenhauer et al., 2023) in 2019–2020, as well as the latest Conductivity/Temperature/Depth (CTD) casts obtained by the NABOS project in 2018 and 2021 (NABOS, https://uaf-iarc.org/nabos). The WOD database contains CTD casts that were mostly obtained in summer ice-free or thin-ice conditions, hydrographic profiles from Ice-Tethered Profilers which provide some coverage of ice-

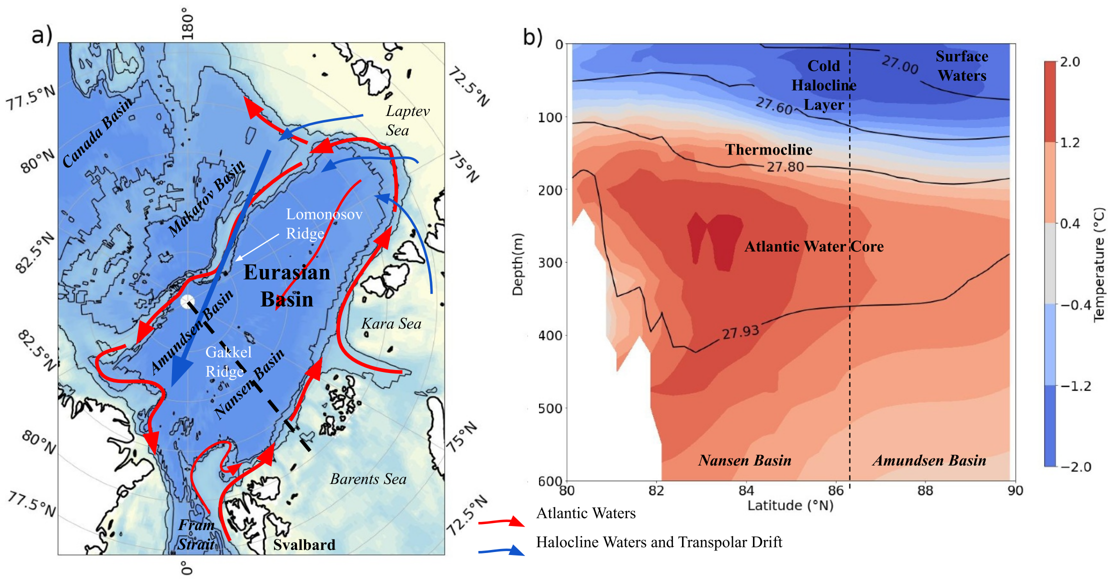

Figure 1. (a) Ocean circulation and main geographic features in the Eurasian Basin. The black dashed line shows the location of the section in (b). (b) Temperature distribution along 40°E between 80°N and 90°N in the World Ocean Atlas climatology. The black contours show the depths of the $\sigma = 27.0$ kg m^{-3}, $\sigma = 27.6$ kg m^{-3}, $\sigma = 27.8$ kg m^{-3}, and $\sigma = 27.93$ kg m^{-3} isopycnals. The dashed line shows the location of the Gakkel ridge, separating the Nansen and Amundsen basins.

covered regions along the Transpolar Drift, in particular during winter, as well as data from Argo floats deployed in the region. In total, our extended data set contains more than 62,000 profiles representing the Eurasian Basin in both summer and winter and covering the period 1987–2023.

Current velocity measurements from the A-TWAIN moorings located on the continental slope of the Nansen Basin at 31°E (Sundfjord et al., 2022) are additionally used in Section 4 to assess the realism of the idealized current velocity distribution used in the conceptual model.

2.2. Methods—Region Definition

To make the profiles comparable with an automated routine, all profiles were interpolated on a regular grid with a 5 m vertical resolution between the surface and 500 m depth. The profiles with an average vertical resolution coarser than 10 m were discarded.

Temperature and salinity profiles exhibit large geographical differences across the Arctic Ocean. In the seasonally ice-free areas north of Svalbard, temperatures can reach up to 4°C in the uppermost 150 m (Meyer et al., 2017) while the same depth range shows temperatures close to the freezing point in the Amundsen Basin (e.g., Metzner & Salzmann, 2023). For the reconstruction of temporal variability of hydrographic properties, it is therefore beneficial to split the Eurasian Basin into smaller regions which undergo comparable changes. While previous studies have used fixed boxes (e.g., Polyakov et al., 2004, 2008), in this study, we define regions based on coherent temperature and salinity profiles.

We use a clustering algorithm to objectively identify profiles representing similar stratification. We apply the K-means algorithm (Hartigan & Wong, 1979), which reduces the variability within each cluster iteratively, to the 15,000 profiles with no missing temperature or salinity data between 20 and 255 m, as the method requires full profiles. To ensure that temperature and salinity variability contribute equally to the clustering process, the profiles are normalized and concatenated into a single combined profile before applying the clustering algorithm. The algorithm is initialized from a prescribed number of random profiles, which are taken as the first centroids. All other profiles are then allocated to the closest of these centroids, based on Euclidean distances between the concatenated T-S profiles, to define the initial clusters. In each cluster, the centroid is then recalculated as the mean of all the cluster members. After a few iterations, the algorithm returns the final clusters. We find that prescribing 8 clusters is sufficient to discriminate between locations with well-known hydrographic contrasts (e.g., the boundary current vs. the basin interior) while making sure that all clusters contain a significant fraction

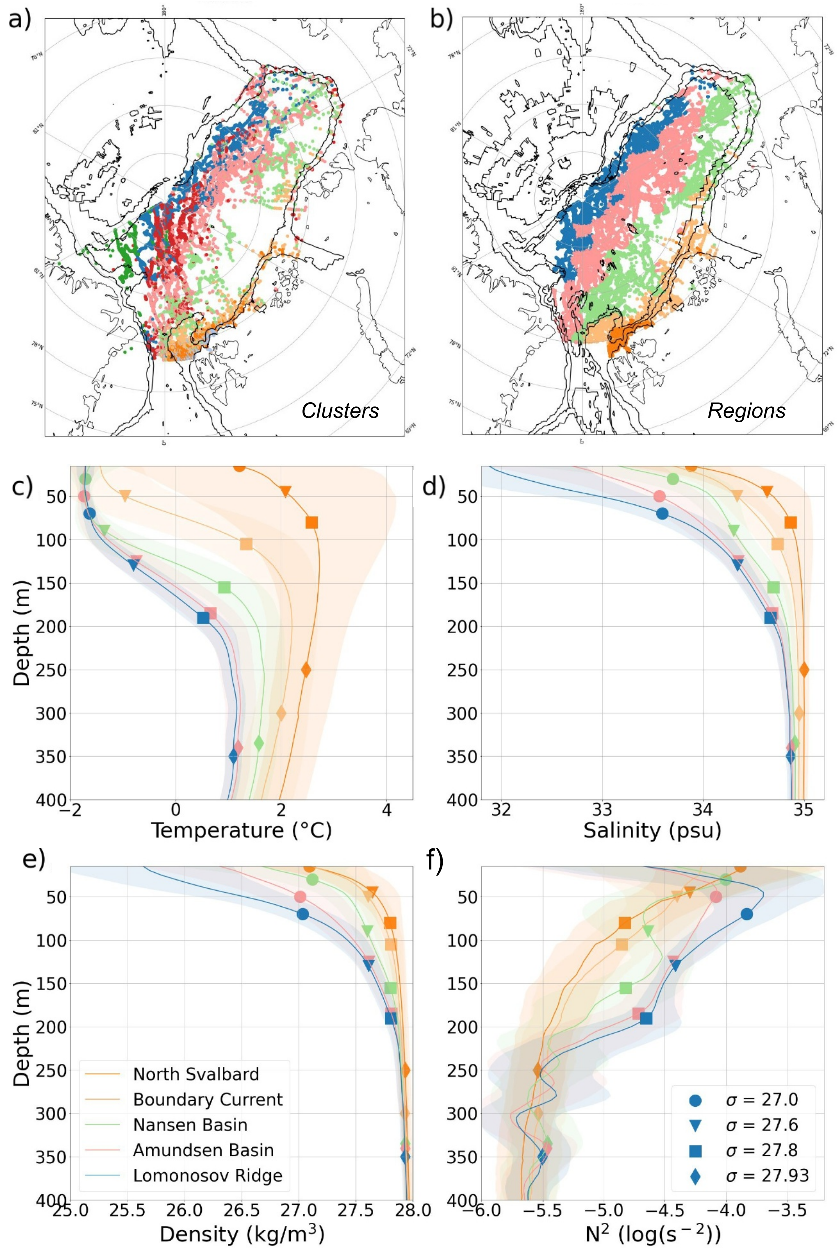

Figure 2. Geographical distribution of (a) the clusters obtained from the 15,000 complete temperature and salinity profiles between 20 and 255 m, and (b) all 62,000 profiles according to their allocated region based on the clusters defined in (a). Region-averaged (c) in situ temperature, (d) salinity, (e) potential density referenced to surface pressure and (f) squared buoyancy frequency associated with the regions in (b). The colors of the profiles correspond to the colors of the regions in (b). Shaded areas show the standard deviations within each region. The colored symbols show the average depths of the $\sigma = 27.0$ kg m^{-3}, $\sigma = 27.6$ kg m^{-3}, $\sigma = 27.8$ kg m^{-3}, and $\sigma = 27.93$ kg m^{-3} isopycnals on each profile.

of the profiles. Figure 2a shows the locations of the 15,000 profiles and their distribution between the 8 clusters. The spatial distribution of the profiles reveals distinct geographic regions between the different clusters such that each cluster is said to represent a region. Similar clusters and geographical distributions can be obtained from separate analysis of summer and winter data, meaning that the seasonality of the data has little impact on cluster allocation (not shown). One exception is the cluster located in the Amundsen Basin, marked with red dots in Figure 2a, which only appears when winter data are included and only contains data from a few specific years showing deeper surface layers in the Amundsen Basin. This cluster has been excluded from the analysis later on. Except for this cluster, the clusters' definition is more influenced by the spatial variability of the profiles than by their time variability, and studying the evolution of water properties in regions defined from these clusters is an effective way to limit the errors stemming from the comparison of profiles from different locations as much as possible.

After defining regions from the initial clustering, our algorithm assigns all 62,000 available profiles—including those used in the clustering step and previously excluded incomplete profiles—to the region corresponding to the dominant cluster within 5° of longitude and 1° of latitude from each profile's location. Furthermore, the gray and orange clusters located north of Svalbard are merged into a single region due to their geographical overlap, and the region associated with the dark green cluster north of Greenland is excluded due to too poor temporal data coverage.

The final region definition used in our analysis is presented in Figure 2b and divides the basin into five regions, whose boundaries match well with the main topographic features of the Eurasian Basin. This matching already suggests that ocean currents, known to be largely affected by the bottom topography at such high latitudes (Isachsen et al., 2003; Karcher et al., 2007), likely play some role in setting the distribution of the hydrographic properties. The regions will be named as follows: (a) North Svalbard (orange region in Figure 2b), (b) Boundary Current (light orange), (c) Nansen Basin (light green), (d) Amundsen Basin (pink) and (e) Lomonosov Ridge (dark blue). In the following sections, we will furthermore use the term "Eurasian Basin interior" when considering the Nansen Basin and Amundsen Basin regions together.

2.3. Construction of Time Series

The available temperature and salinity profiles were used to reconstruct time series of monthly hydrographic properties at various depths of the water column over the period 1987–2023. As expected, the intra-annual temporal distribution of the data is highly uneven at all depths, with a notably larger number of profiles collected during the warm season. This uneven distribution could bias estimates of the long-term variability and would, in principle, require at least a deseasoning of the data. However, we found that—except in the surface layer—the seasonal cycle is relatively weak compared to the spatial variability within each region and is difficult to estimate reliably. We therefore chose to construct time series using raw monthly data rather than deseasoned data. Alternative approaches based on time series for individual seasons were also considered. Only the summer and fall seasons were adequately sampled, and the resulting time series exhibited variability similar to that of the full-year time series.

To avoid temperature and salinity biases linked to the variable geographic distribution of available data within a region from 1 month to the next, each temperature and salinity profile was compared to the annual World Ocean Atlas (WOA) climatology with a 1° resolution (https://www.nodc.noaa.gov/OC5/woa18/, see Locarnini et al., 2013; Zweng et al., 2019) at the closest grid point to calculate anomalies from the climatology. At various depths, all anomalies for a given month in a given region were then averaged to build a time series of the temperature and salinity anomalies. Outliers, defined as anomalies which spread out from the long-term trend by more than two standard deviations, were then removed from all time series. The correction of the biases induced by the geographic distribution of profiles within a region could not be applied to the squared buoyancy frequency, due to the presence of unstable profiles in the WOA climatology.

Estimates of the uncertainties on the trends were calculated following Storch (1998), as:

$$[a + t_{2.5\%} s_a; a + t_{97.5\%} s_a]$$

with:

$$s_a^2 = \frac{s_r^2}{n s_t^2}$$

where a is the estimated trend, $t_{2.5\%}$ and $t_{97.5\%}$ are the 2.5% and 97.5% percentiles for a Student law with n degrees of freedom, n is estimated from Santer et al. (2000), s_r^2 is the variance of the detrended time series and s_t^2 is the variance of the time values with available data.

3. Results: Enhanced Warming and Salinity Increase in the Thermocline and Large-Scale Weakening of Stratification in the Thermocline Down to the AW Core

3.1. Regional Contrasts in the Stratification Profiles

The typical stratification in the Arctic Ocean has some key features that are present in all identified regions: (a) a surface layer, characterized by temperatures close to the freezing point and low salinities compared to deeper layers—not visible in Figure 2 due to the averaging of summer and winter profiles; (b) the CHL; (c) the so-called thermocline and (d) the AW core. The colored symbols in Figures 2c–2f show the depths of the $\sigma = 27.0$ kg m^{-3}, $\sigma = 27.6$ kg m^{-3}, $\sigma = 27.8$ kg m^{-3} and $\sigma = 27.93$ kg m^{-3} isopycnals in all regions, representing the boundaries between these layers.

The average temperature and salinity profiles for each region presented in Figures 2c and 2d provide an overview of the T-S spatial variability across the Eurasian Basin. The North Svalbard region features warm and saline profiles, with maximum AW temperatures of 2.5–4°C located relatively close to the surface, between 50 and 100 m. Downstream in the Boundary Current region, surface temperatures have cooled down to values close to the freezing point and the AW core has moved down to almost 200 m. The stratification shows little change between the North Svalbard and the Boundary Current regions, as the effects of cooling and freshening at the surface compensate each other. In these regions, a seasonal halocline is formed by the pronounced salinity difference between AW and summer meltwater. In winter, the halocline is removed as a result of surface freezing, subsequent brine release, and mixing with AW (Baumann et al., 2018; Fer et al., 2017; Metzner & Salzmann, 2023). The transition from the Boundary Current region to the Nansen Basin region is characterized by a deepening of the 27.6 kg m^{-3} isopycnal, representing the lower boundary of the CHL, down to 100 m. The thermocline also deepens between the two regions from approximately 100 m in the Boundary Current region to about 150 m in the Nansen Basin (Figure 2). The thermocline deepening comes along with a decrease in temperature and salinity. From the Nansen Basin to the Amundsen Basin, the AW core continues to cool and descend—it reaches 300 m depth in the Amundsen Basin. The CHL stratification increases, due to lower salinities in the uppermost 150 m, and is maintained throughout the year. The difference between the Amundsen Basin and Lomonosov Ridge regions is mostly driven by salinity changes in the first 100 m. Almost 1 Sv of relatively fresh waters from the Siberian shelves is transported into the Eurasian Basin by the surface-intensified Transpolar Drift. This transport is confined to the uppermost 50 m (Charette et al., 2020), which significantly lowers subsurface salinities in the Lomonosov Ridge region. Across the entire Eurasian Basin, density profiles have the same shape as salinity profiles which emphasizes the important role of salinity for the stratification in the Eurasian Basin. The spatial variability of the depths of the boundaries between the surface layer, the CHL, the thermocline and the AW core are summarized in Figure S1.

3.2. Low-Frequency Temperature and Salinity Variability in the Thermocline Above the AW Core

Figure 3 presents the evolution of the temperature and salinity in all regions since the mid-1980s. Long-term trends in temperature and salinity are most visible in the Eurasian Basin interior. Figures 3c and 3d show significant multi-decadal warming and salinification trends, which are particularly pronounced in the thermocline. The largest temperature increase is found at 150 m in the Nansen Basin where it reaches 0.4°C (±0.1°C at the $p = 0.05$ significance level) per decade. In the Amundsen Basin, the temperature trend in the thermocline is mostly visible from the year 2000. In the meantime, the salinity at the CHL base (between 100 and 150 m) has increased significantly, by 0.1 psu (±0.05 psu at the $p = 0.05$ significance level) per decade in both the Nansen Basin and Amundsen Basin regions.

In the other regions, located along the edges of the basin, the temperature and salinity variability is impacted by the passage of warm and saline anomalies persisting over several years, potentially superimposed on the long-term trends. An example of warm and saline anomaly is observed in the North Svalbard region between 2004 and 2008 (Figure 3a) and can be found a few years later in the Boundary Current region (Figure 3b). Signs of other warm anomalies may be visible in the North Svalbard region in 1992–94 and 2014–16. The larger error bars in Figures 3a and 3b compared to the other panels are likely due to the small-scale horizontal variability between the core of the AW current, which is typically 30 km wide north of Svalbard (Perez-Hernández et al., 2017; Våge et al., 2016), and the rest of the regions. Still, a significant positive temperature trend can be identified in the North Svalbard and Boundary Current regions at most depths (see Figure 4), with the fastest increase at 100 m.

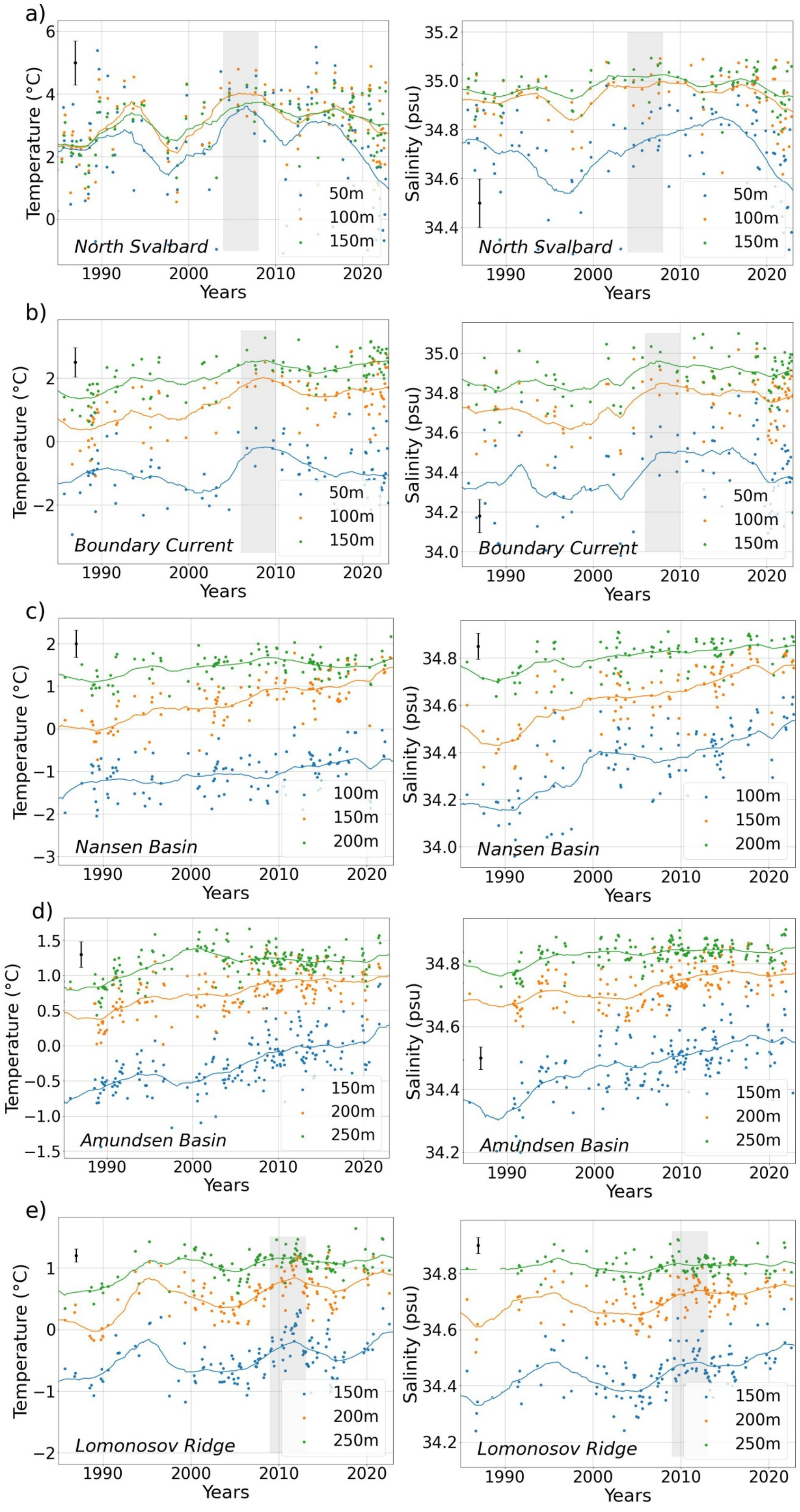
a)
Temperature (°C)
Salinity (psu)
North Svalbard
50m
100m
150m
Years
b)
Boundary Current
c)
Nansen Basin
100m
150m
200m
d)
Amundsen Basin
150m
200m
250m
e)
Lomonosov Ridge

Figure 3.

The different variability patterns observed in the Amundsen Basin and Lomonosov Ridge regions are a good illustration of the contrasts between the basin edges and its interior. At least two periods of higher temperatures and salinities are observed in the Lomonosov Ridge region: a first one in the 1990s, whose timing and amplitude are difficult to estimate accurately due to poor data coverage, and a second one peaking in 2011. These anomalies are most pronounced in the thermocline, with typical amplitudes of 0.5°C and 0.1 psu, and remain relatively weak close to the AW core (250 m), though following a similar pattern. The 1990s' warm period in the Lomonosov region could be associated with the arrival of the anomaly identified by Quadfasel et al. (1991) (Morison et al., 1998), and the later warm and saline periods could correspond to the passage of more recent warm anomalies that were so far only detected from Fram Strait to the Eastern Eurasian Basin, with a lag of around 5 years between Fram Strait and the Lomonosov Ridge region. Despite the presence of these anomalies, significant positive temperature and salinity trends (+0.3°C (±0.2°C at $p = 0.05$) per decade at 200 m and +0.09 psu (±0.02 psu at $p = 0.05$) per decade at 150 m) are still visible from the early 2000s. The presence of an anomaly in the 1990s and data scarcity make it harder to extend this trend back to the 1980s, although available data suggest the potential existence of a long-term trend starting in the late 1980s (Figures 3 and 4).

3.3. Vertical Migration of Isopycnals and Large-Scale Weakening of Stratification

Since the stratification in the Arctic is mostly salinity-driven above the AW layer, the stratification in this layer is likely to be impacted by the positive salinity trends which are observed in most of the Eurasian Basin (from the Nansen Basin to the Lomonosov Ridge) close to the CHL base. Figure 5 shows the evolution of the $\sigma = 27.0$, 27.6, 27.8, and 27.93 kg m^{-3} isopycnal depths, providing a visualization of stratification changes over more than 30 years.

The $\sigma = 27.6$ kg m^{-3} and $\sigma = 27.8$ kg m^{-3} isopycnals are found to have moved upwards since the 1980s in the Nansen Basin and Amundsen Basin regions, with an average pace of 15 m (±8 m) per decade. In the Lomonosov Ridge region, similar trends are observed from the 2000s. These isopycnal movements are due to the large positive salinity trends observed in the thermocline and at the base of the CHL. Further up, no significant trends are found in the depth of the $\sigma = 27.0$ kg m^{-3} isopycnal, meaning that the isopycnals located in the CHL have moved closer together. Concomitantly, below the AW core, the depth of the $\sigma = 27.93$ kg m^{-3} isopycnal is found to increase over time at a pace of 37 m (±26 m at $p = 0.05$) per decade in the Boundary Current and 17 m (±9 m at $p = 0.05$) per decade in the Amundsen Basin. In the other regions, the trend is weakly significant. Therefore the isopycnals located above and below the AW core tend to move apart from each other in all five regions, implying a general weakening trend in the stratification of the AW layer. In the Amundsen Basin region for example, the thickness of the AW core, bounded by the $\sigma = 27.8$ kg m^{-3} and the $\sigma = 27.93$ kg m^{-3} isopycnals, doubled between 1990 and 2020, increasing from less than 100 m to more than 200 m (Figure 5d). As a result, the mean stratification in this layer decreased by 50% in 30 years (Figure 4).

The temperature, salinity and stratification trends and their uncertainties are summarized in Figure 4 and Table 1. Though a depth range with a significant warming and salinity increase can be identified in most regions, the largest trends and lowest uncertainties are found in the Nansen and Amundsen Basin regions (Figures 4c and 4d). The depths of largest temperature and salinity increases match the depths of the largest vertical temperature and salinity gradients in the mean profiles. This corresponds to an upward migration of the full thermocline rather than an increase of the temperature of the AW core, and to an upward migration of the base of the CHL. Stratification changes are only significant in the Eurasian Basin interior. There, the layers with a reduced stratification span from the CHL base (50–100 m) to below the AW core (around 350 m), with stratification decreasing at rates mostly between 1% and 3% per year. This weakening of the stratification is mostly salinity-driven. Below 350 m, the sign of the stratification trend switches and a significant stratification increase is visible in most regions. This stratification increase is temperature-driven and can be associated with a faster temperature increase of the AW core compared to deeper waters. A subsurface stratification increase is also visible close to 50 m, significant at

Figure 3. Time series of monthly temperatures (left) and salinities (right) over the period 1987–2023 at different depths above the Atlantic Water core in (a) the North Svalbard (at 50, 100, and 150 m), (b) the Boundary Current (at 50, 100, and 150 m), (c) the Nansen Basin (at 100, 150, and 200 m), (d) the Amundsen Basin (at 150, 200, and 250 m) and (e) the Lomonosov Ridge (at 150, 200, and 250 m) regions. Solid lines show a weighted average of monthly values computed over 8-year-long windows, with decreasing weights toward the window's edges. The black error bars show the average standard deviation of temperature and salinity values used for monthly averages. The shaded areas show the estimated timing of the propagation of a warm and saline anomaly along the basin edges.

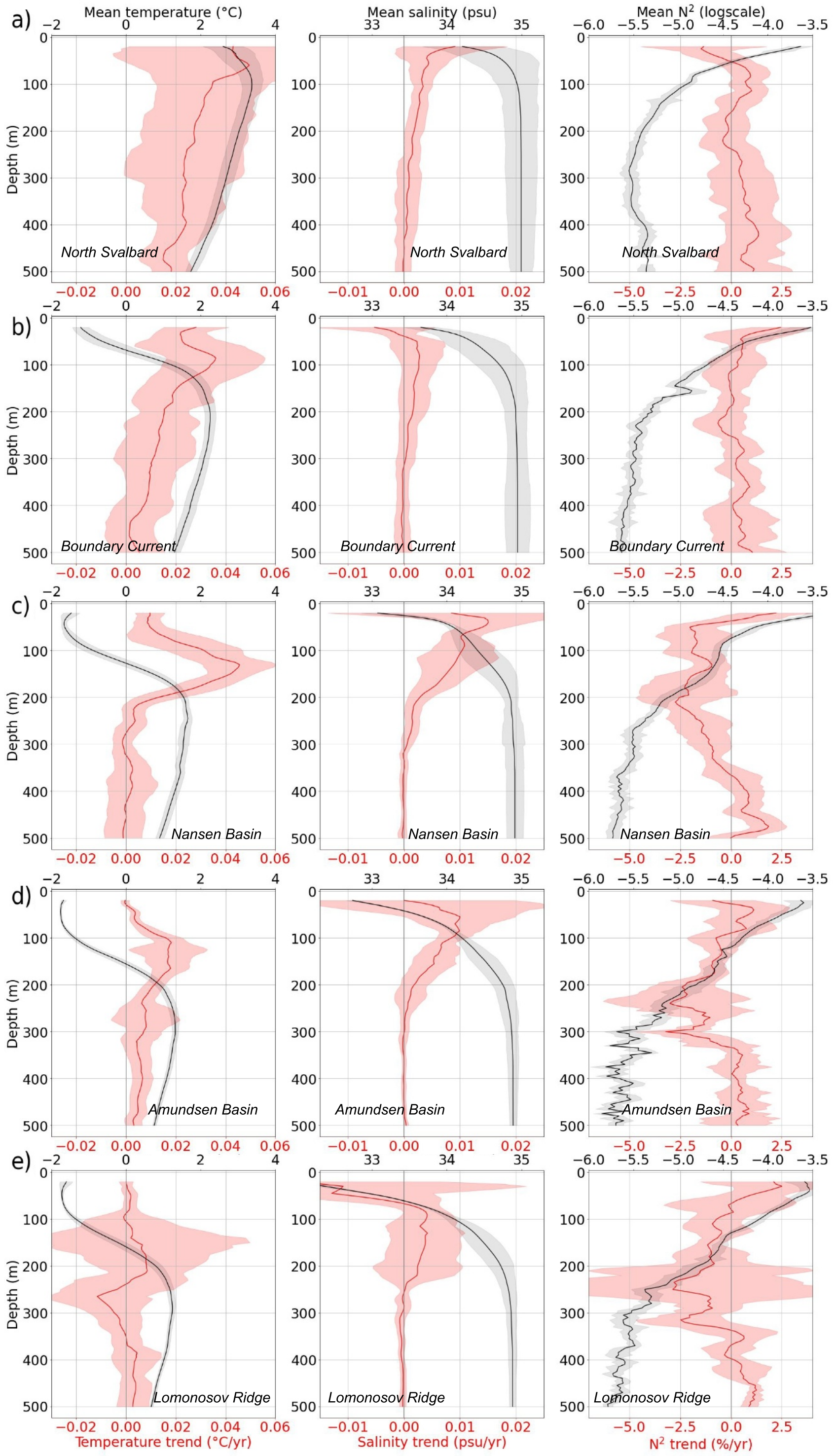

Figure 4. Mean profiles (in black) and trends (in red) over the period 1987–2023 for (left) temperature, (middle) salinity and (right) squared buoyancy frequency in (a) the North Svalbard, (b) the Boundary Current, (c) the Nansen Basin, (d) the Amundsen Basin and (e) the Lomonosov Ridge regions. The shaded areas show the 95% confidence intervals. The top (resp. bottom) horizontal axes refer to the mean state (resp. the trends).

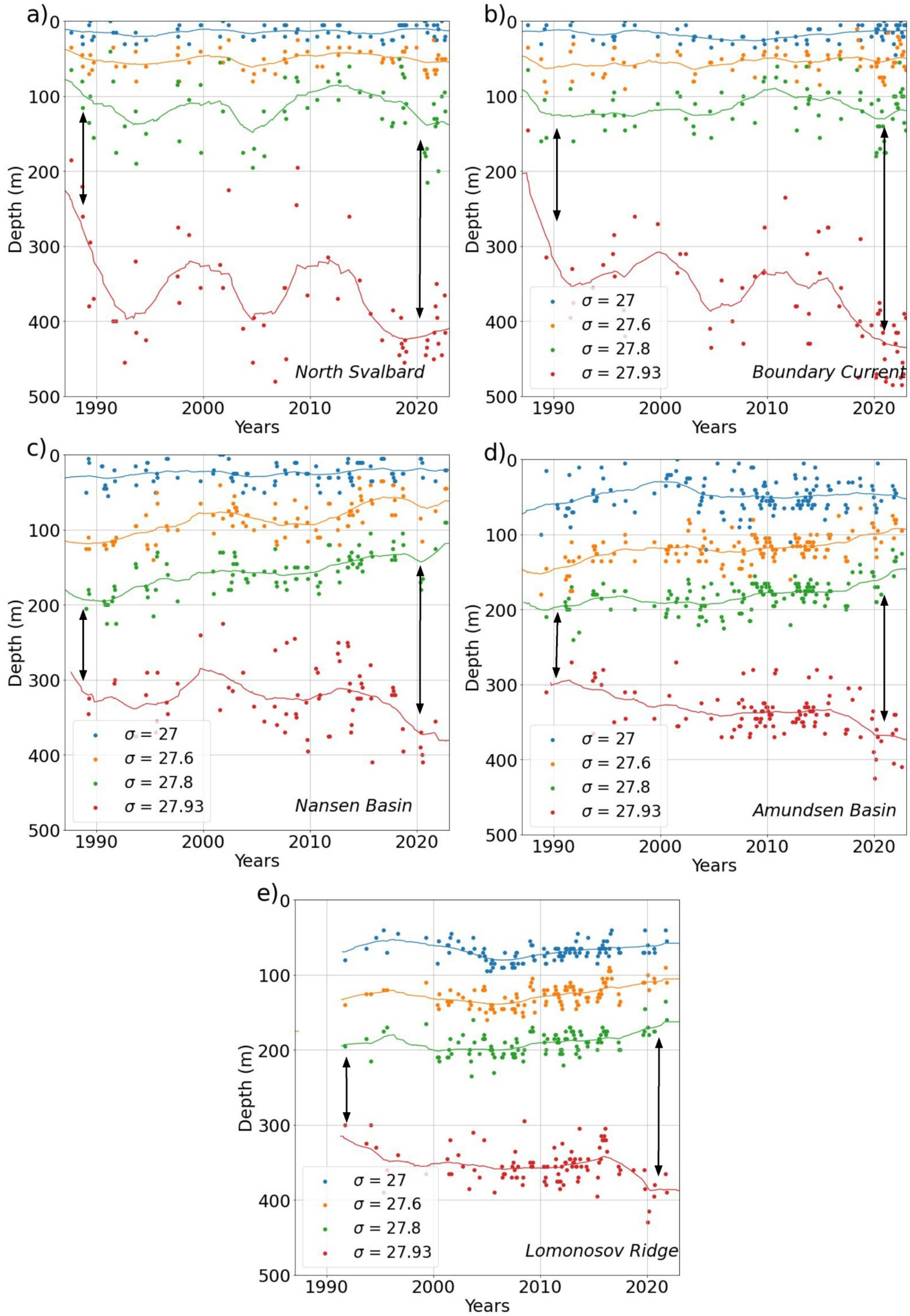

Figure 5. Monthly depths of the $\sigma = 27.0$ kg m^{-3}, $\sigma = 27.6$ kg m^{-3}, $\sigma = 27.8$ kg m^{-3}, and $\sigma = 27.93$ kg m^{-3} isopycnals in (a) the North Svalbard, (b) the Boundary Current, (c) the Nansen Basin, (d) the Amundsen Basin and (e) the Lomonosov Ridge regions. Solid lines show a weighted average of monthly values computed over 8-year-long windows, with decreasing weights toward the window's edges.

95% in the Nansen Basin and the Lomonosov Ridge regions. It is salinity-driven and associated with a faster salinity increase at the CHL base compared to the surface, where no significant salinity trends are found.

In this section, we documented the variability in the T-S properties of the AW and upper layers in the Eurasian Basin. We found that regions located in the basin interior (Nansen Basin and Amundsen Basin regions) experienced a long-term warming and salinification trend, while on the edges of the basin (North Svalbard, Boundary

Table 1
Summary of the Main Trends Identified From Figure 4 in the Eurasian Basin Over the 1987–2023 Period

Region	Depth range with significant temperature trend	Maximum temperature trend (°C/yr)	Depth range with significant salinity trend (m)	Maximum salinity trend (psu/yr)	Depth range with significant stratification trend	Maximum stratification trend (%/yr)
North Svalbard	20–500 m	+0.05 (±0.03) at 50 m	50–250	+0.004 (±0.003) at 50 m	N.A.	N.A.
Boundary Current	20–400 m	+0.035 (±0.015) at 100 m	100–120	+0.0025 (±0.0025) at 100 m	N.A.	N.A.
Nansen Basin	20–220 m	+0.045 (±0.012) at 140 m	30–280	+0.015 (±0.005) at 50 m	50–350 m (negative)	−2.6 (±1.4) at 220 m
					400–480 m (positive)	+1.8 (±0.8) at 470 m
Amundsen Basin	40–260 m	+0.017 (±0.007) at 100–170 m	50–200	+0.01 (±0.003) at 90 m	140–310 m (negative)	−3 (±2) at 240 m
	350–500 m				400–410 m (positive)	+0.6 (±0.4) at 470 m
Lomonosov Ridge	N.A.	N.A.	80–100	+0.004 (±0.004) at 120 m	140–160 and 300–320 m (negative)	−2.6 (±4.4) at 250 m
					440–500 m (positive)	1.1 (±0.2) at 460 m

Note. The values in brackets indicate the 95% uncertainty intervals for the trend estimates.

Current, and Lomonosov Ridge regions), several shorter warm and saline anomalies were superimposed on existing trends. Both short-term anomalies and long-term trends in the temperature and salinity were found to be concentrated in the thermocline and at the CHL base rather than close to the AW core in the Eurasian Basin. Associated with this signal, a reduced stratification was observed in the thermocline and upper AW core in all regions, as well as a thickening of the AW core, bounded by the $\sigma = 27.8$ kg m^{-3} and the $\sigma = 27.93$ kg m^{-3} isopycnals.

4. A Conceptual Model of Weakening Stratification and Thickening AW Core

4.1. Description of the Conceptual Model

We postulate that anomalies identified along the edges of the Eurasian Basin are advected from the basin entrance. To test this hypothesis, we use a simple advective-diffusive model to examine how vertical diffusion of temperature and salinity anomalies could transform anomalies entering through Fram Strait along their pathway, and account for their accumulation in the thermocline as described in Section 3. Our model takes into account what we consider the main features regulating the evolution of temperature and salinity anomalies in the basin: a subsurface salinity-stratified layer, which contains a thermocline extending down to the AW core and is capped by a cold, fresh surface layer, and an advective component representing the large-scale circulation of the boundary current. The Lagrangian equations driving the evolution of the temperature T and salinity S of a water column circulating around the basin may be written as follows (Equation 1):

$$\frac{DT(z,t)}{Dt} = \Gamma \frac{\partial}{\partial z}\left(\frac{\varepsilon(z)}{N^2(z,t)}\frac{\partial T(z,t)}{\partial z}\right) + F(z,t) \tag{1}$$

$$\frac{DS(z,t)}{Dt} = \Gamma \frac{\partial}{\partial z}\left(\frac{\varepsilon(z)}{N^2(z,t)}\frac{\partial S(z,t)}{\partial z}\right) + G(z,t)$$

$$N^2(z,t) = \frac{-g}{\rho_0}\frac{\partial \rho(S,T)}{\partial z}$$

Diffusion is modeled here using the Osborn relation (Osborn, 1980) commonly used for turbulent heat fluxes (Lenn et al., 2011; Meyer et al., 2017), which expresses the turbulent diffusivity as (Equation 2):

$$K_z = \Gamma \frac{\varepsilon}{N^2} \tag{2}$$

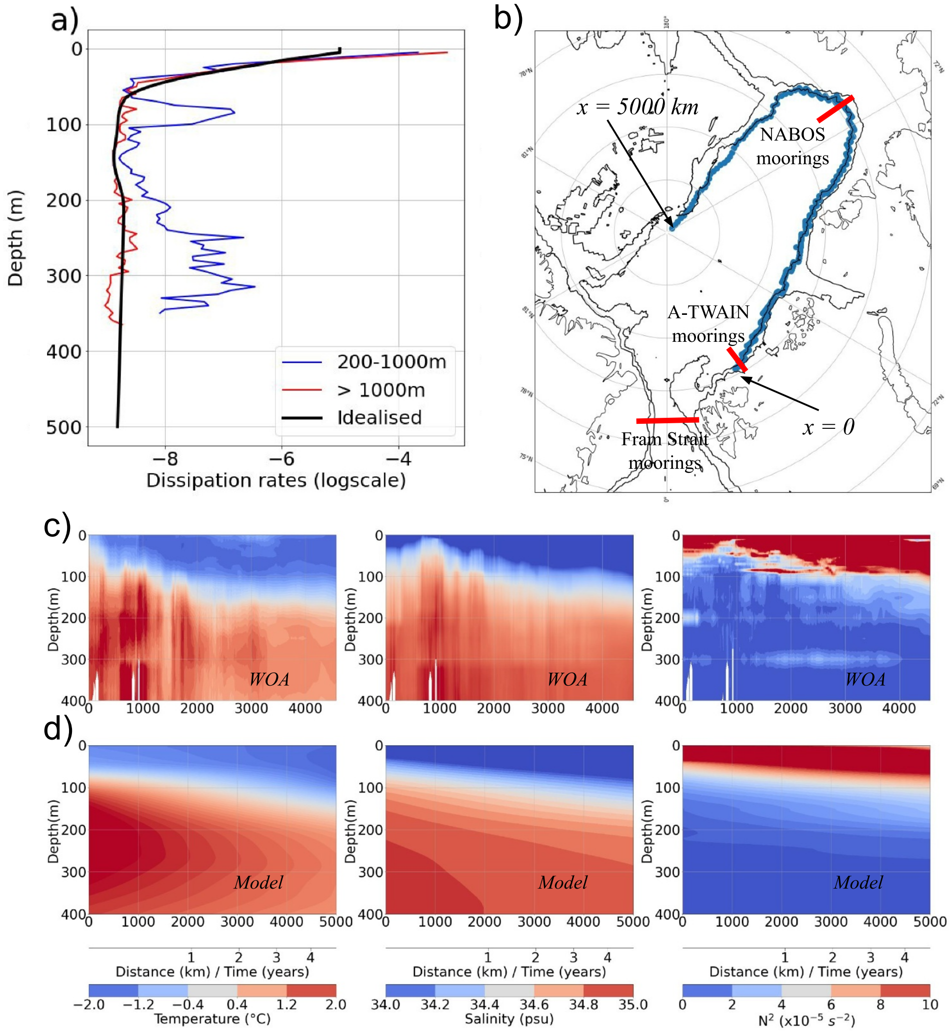

Figure 6. (a) Microstructure measurements during Akademik Tryoshnikov cruise AT2018 along the boundary current between 100°E and 150°E over depths shallower (blue) and deeper (red) than 1,000 m, shown with the idealized dissipation rate used in the conceptual model (black). (b) Trajectory of the water column in the conceptual model (blue) and location of the Fram Strait, A-TWAIN, and NABOS mooring lines (red lines). (c, d) Temperature, salinity, and squared buoyancy frequency profiles along the pathway of the water column in (c) the World Ocean Atlas climatology and (d) the reference state of the conceptual model.

where ε is the dissipation rate, N^2 is the squared buoyancy frequency and Γ is the mixing efficiency, usually set to 0.2. With this formulation, we neglect other vertical diffusive processes such as double diffusion. F and G are forcing terms accounting for all other processes affecting the temperature and salinity.

The profile of the dissipation rate ε is chosen based on microstructure measurements collected along the path of the boundary current in 2018 (Schulz et al., 2022), with values close to 10^{-5} W/kg at the surface and decaying to 10^{-9} W/kg between 100 and 1,000 m. According to observations collected during the Akademik Tryoshnikov cruise AT2018 in 2018, these values are up to two orders of magnitude lower than the dissipation rates at the shelf break (in blue in Figure 6a) and closer to profiles further offshore (in red in Figure 6a), where most of our observations are located. The water column in the model travels 5,000 km following the edges of the basin at the velocity v, which is assumed to be barotropic (Equation 3):

$$v(x) = 14e^{\frac{-x}{1,000}} + 2, \tag{3}$$

where x is the distance from the entrance following the water column pathway expressed in km and v is expressed in cm/s. Equation 3 assumes an exponential decrease of the velocity with distance from the basin entrance, from 16 cm/s at the entrance to 2 cm/s close to the North Pole, to account for the downslope migration and slowdown of the Fram Strait branch of the boundary current while passing Saint Anna Trough (Ruiz-Castillo et al., 2023). The characteristic decay scale corresponds to a transit time of 5 years around the basin, consistent with values suggested by Swift et al. (1997) and results of Section 3, where warm anomalies were found to travel between the North Svalbard and the Lomonosov Ridge regions in around 5 years (compare Figures 3a and 3e). The velocity at the basin entrance is slightly larger than the average velocity of 12 cm/s observed in the core of the current at the A-Twain mooring line (Athanase et al., 2020) and velocities along the Lomonosov Ridge are similar to those found by Aagaard (1989). Note that the model results were found to be almost insensitive to changes in the shape of the velocity profile in Equation 3, or to an increase in the advection timescale to values up to 15 years.

The model is used to predict how temperature and salinity anomalies at the basin entrance are modified while circulating around the basin. These anomalies (T', S', $N^{2\prime}$) are defined as the difference between a perturbed state (T_a, S_a, N_a^2) and an evolving reference state (T_{ref}, S_{ref}, N_{ref}^2) based on the climatological ocean conditions along the anomalies' pathway. Supposing that the only changes between the two states of the system are the result of vertical diffusion and advection—or in other words that the forcings F and G stay the same, the equations of the temperature and salinity anomalies can be obtained as (Equation 4):

$$\begin{aligned}
\frac{DT'}{Dt} &= \Gamma\left[\frac{\partial}{\partial z}\left(\frac{\varepsilon}{N_a^2}\frac{\partial T_a}{\partial z}\right) - \frac{\partial}{\partial z}\left(\frac{\varepsilon}{N_{\mathrm{ref}}^2}\frac{\partial T_{\mathrm{ref}}}{\partial z}\right)\right] \\
\frac{DS'}{Dt} &= \Gamma\left[\frac{\partial}{\partial z}\left(\frac{\varepsilon}{N_a^2}\frac{\partial S_a}{\partial z}\right) - \frac{\partial}{\partial z}\left(\frac{\varepsilon}{N_{\mathrm{ref}}^2}\frac{\partial S_{\mathrm{ref}}}{\partial z}\right)\right] \\
N^{2\prime} &= N_a^2 - N_{\mathrm{ref}}^2
\end{aligned} \tag{4}$$

Or, expressed in terms of anomalies (Equation 5):

$$\begin{aligned}
\frac{DT'}{Dt} &= \Gamma\frac{\partial}{\partial z}\left(\frac{\varepsilon}{N_{\mathrm{ref}}^2 + N^{2\prime}}\frac{\partial T'}{\partial z}\right) - \Gamma\frac{\partial}{\partial z}\left(\frac{\varepsilon N^{2\prime}}{N_{\mathrm{ref}}^2\left(N_{\mathrm{ref}}^2 + N^{2\prime}\right)}\frac{\partial T_{\mathrm{ref}}}{\partial z}\right) \\
\frac{DS'}{Dt} &= \Gamma\frac{\partial}{\partial z}\left(\frac{\varepsilon}{N_{\mathrm{ref}}^2 + N^{2\prime}}\frac{\partial S'}{\partial z}\right) - \Gamma\frac{\partial}{\partial z}\left(\frac{\varepsilon N^{2\prime}}{N_{\mathrm{ref}}^2\left(N_{\mathrm{ref}}^2 + N^{2\prime}\right)}\frac{\partial S_{\mathrm{ref}}}{\partial z}\right) \\
N^{2\prime} &= N_a^2(T', S') - N_{\mathrm{ref}}^2
\end{aligned} \tag{5}$$

If the anomalies T', S', and $N^{2\prime}$ are small compared to the reference values T_{ref}, S_{ref}, and N_{ref}^2, these equations can be linearized around the reference state as (Equation 6):

$$\begin{aligned}
\frac{DT'}{Dt} &\simeq \Gamma\frac{\partial}{\partial z}\left(\frac{\varepsilon}{N_{\mathrm{ref}}^2}\frac{\partial T'}{\partial z}\right) - \Gamma\frac{\partial}{\partial z}\left(\frac{\varepsilon N^{2\prime}}{N_{\mathrm{ref}}^4}\frac{\partial T_{\mathrm{ref}}}{\partial z}\right) \\
\frac{DS'}{Dt} &\simeq \Gamma\frac{\partial}{\partial z}\left(\frac{\varepsilon}{N_{\mathrm{ref}}^2}\frac{\partial S'}{\partial z}\right) - \Gamma\frac{\partial}{\partial z}\left(\frac{\varepsilon N^{2\prime}}{N_{\mathrm{ref}}^4}\frac{\partial S_{\mathrm{ref}}}{\partial z}\right) \\
N^{2\prime} &\simeq -g\frac{\partial(\alpha(T_{\mathrm{ref}}, S_{\mathrm{ref}})\,T')}{\partial z} + g\frac{\partial(\beta(T_{\mathrm{ref}}, S_{\mathrm{ref}})\,S')}{\partial z}
\end{aligned} \tag{6}$$

where α and β are the seawater thermal expansion and haline contraction coefficients respectively.

Equation 6 is used for the interpretation of physical processes in Figure 9 while Equation 5 is the one implemented in the model. These equations assume that the evolution of tracer (either T or S) anomalies along their pathway is balanced by two diffusion-like terms. The first term corresponds to the diffusion of anomalies in the mean

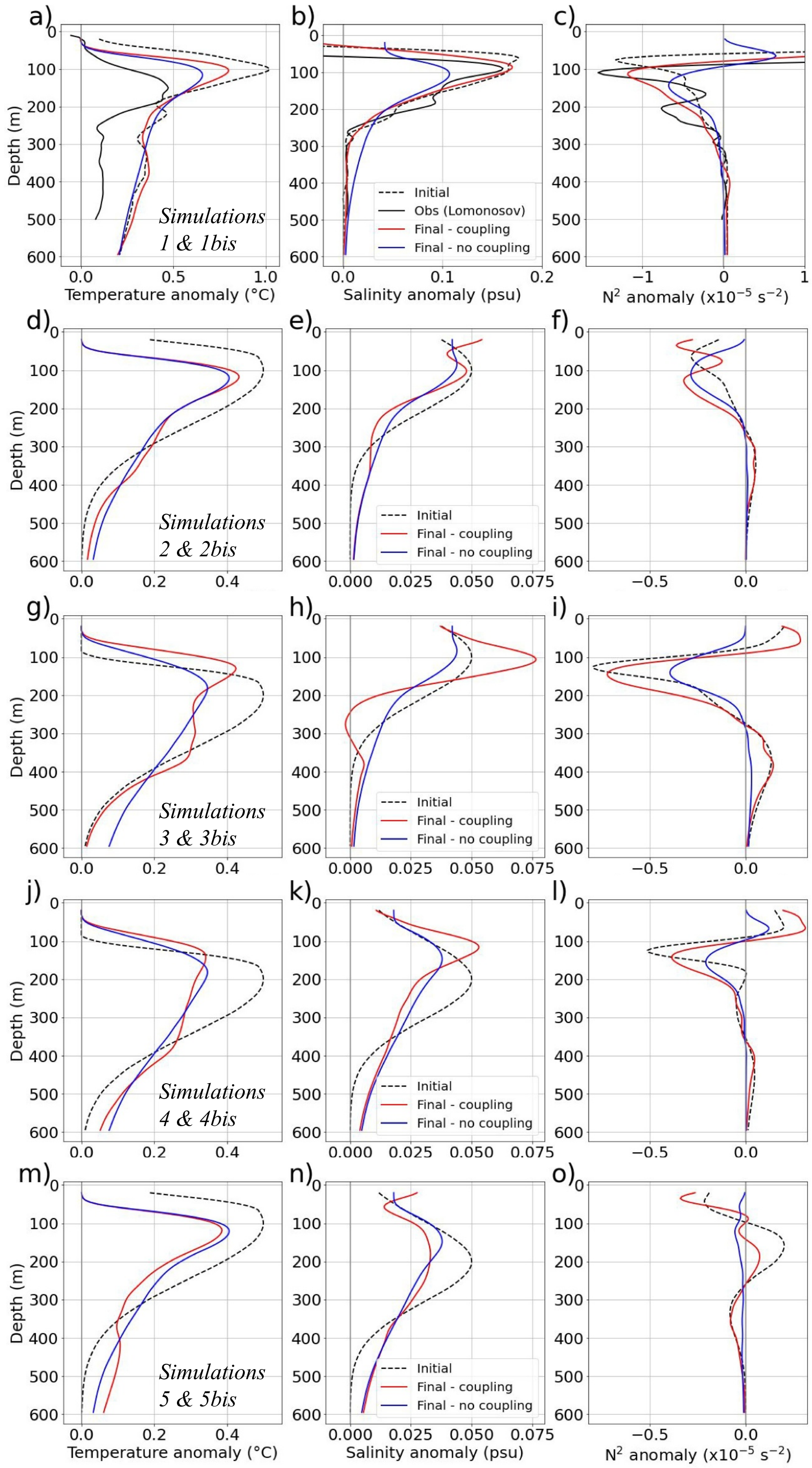

Figure 7. Synthesis of the initial (dashed) and final (solid) anomaly profiles in all 10 simulations. Each panel summarizes the final profiles obtained from two simulations with the same initial conditions but including (red) or ignoring (blue) the coupled term in the integration of Equation 5. The solid black profiles in (a–c) show the anomalies in the Lomonosov Ridge region estimated from the observations.

Table 2
Summary of the 10 Simulations With the Conceptual Model

Simulations	1	1bis	2	2bis	3	3bis	4	4bis	5	5bis
Depth of the maximum of the initial temperature anomaly (m)	100 (obs.)	100 (obs.)	100	100	200	200	200	200	100	100
Depth of the maximum of the initial salinity anomaly (m)	70 (obs.)	70 (obs.)	100	100	100	100	200	200	200	200
Inclusion of the "coupled term"	Yes	No	Yes	No	Yes	No	Yes	No	Yes	No

Note. Simulations 1 and 1bis are initialized with anomaly profiles calculated from the observations as the difference between the 1999–2004 and 2006–2009 periods. In simulations 2/2bis to 5/5bis, the maximum of the initial anomalies is 0.5°C and 0.05 psu, respectively, and the vertical extent is 200 m for the temperature anomaly and 150 m for the salinity anomaly.

stratification. It is responsible for a vertical spreading of the *T-S* anomalies entering the basin and will thereafter be referred to as "the uncoupled term." The second term corresponds to the anomalous diffusion of the mean profile due to stratification changes induced by changes in the tracer profiles. It will thereafter be referred to as "the coupled term" as it accounts for the coupling between *T-S* anomalies and stratification anomalies.

We consider the evolution of anomalies initially present in the Boundary Current region (as defined in Figure 2b) down to the Lomonosov Ridge region, along the path shown in Figure 6b. Solving Equation 5 for given initial anomalies requires the knowledge of the reference state (T_{ref}, S_{ref}, N^2_{ref}). The latter is obtained by linear interpolation between the profiles representing the start and end points of this path, respectively. By comparison with observational data from the WOA climatology, we find that this is a simplified, but realistic representation of the reference state (Figures 6c and 6d) while offering the advantage of a smoother evolution of the conditions along the anomaly path.

The boundary conditions assume no temperature anomaly at the surface and zero salinity flux anomaly through the surface. The temperature condition therefore allows some anomalous heat loss at the surface. The model bottom boundary condition imposes no temperature and salinity anomalies at a depth of 1,000 m. Testing different boundary conditions (zero salinity anomaly at the surface or no anomalous heat flux through the surface) did not yield qualitatively different results regarding the impact of anomalies on the stratification in the AW layer.

We first test how the model transforms realistic *T-S* profiles observed in the Boundary Current region during a warm anomaly and compare these results to observed anomaly profiles in the Lomonosov Ridge region (simulations 1/1bis). Initial anomaly profiles in these simulations are calculated as the difference between the mean profiles of the 1999–2004 period (pre-anomaly conditions) and the 2006–2009 period (detection of the anomaly in the observations) in the Boundary Current region. They are characterized by a maximum of the temperature anomaly at 100 m, and a maximum of the salinity anomaly at 70 m (Table 2). The shallower salinity anomaly compared to the temperature anomaly induces a weakening of stratification in the thermocline, below the salinity anomaly maximum (Figure 7c).

Because the AW core was shown to sink from 100 to 300 m between the basin entrance and the Lomonosov Ridge (Figure 2c), we then run four idealized simulations with deeper initial *T-S* anomalies, testing the evolution of anomalies after they have sunk with the AW core. We further test the role of the depth difference between the initial temperature and salinity anomaly maxima, by running simulations where the initial temperature anomaly is above, at the same depth or below the initial salinity anomaly (Table 2, simulations 2/2bis to 5/5bis). These four idealized simulations are initialized with temperature and salinity anomalies at either 100 m or 200 m. The anomalies are shaped as skewed Gaussian functions with maxima of 0.5°C and 0.05 psu for temperature and salinity, respectively (Figures 7 and 8), in agreement with the magnitude of observed anomalies at the basin entrance. Simulations with these five different initial anomalies are run twice, once ignoring the "coupled term" and once taking both terms of Equation 5 into account (Table 2).

4.2. Response of the Water Column to Temperature and Salinity Anomalies

Figures 7a–7c provide a comparison of the evolution of realistic anomaly profiles in the model with observations of anomalies in the Lomonosov Ridge region, a few years after their detection at the basin entrance. Observed anomaly profiles in the Lomonosov Ridge region (solid black curves) are calculated as the difference between the mean *T-S* profiles of the 2002–2007 and 2009–2012 periods. They are characterized by a concentration of *T-S*

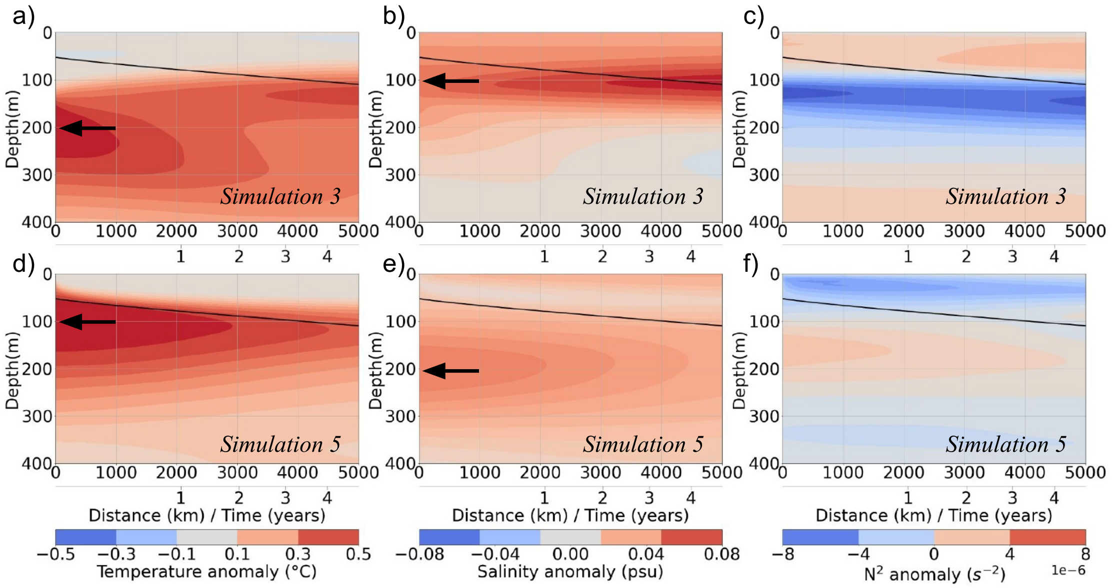

Figure 8. Vertical distribution of the (a, d) temperature, (b, e) salinity and (c, f) squared buoyancy frequency anomalies along the water column pathway for simulations 3 and 5 (simulations with the coupled term). The black line on all plots indicates the base of the cold halocline layer ($\sigma = 27.6$ kg m^{-3} isopycnal) and the black arrows indicate the depths of the maximum initial temperature and salinity anomalies.

anomalies in the thermocline and at the CHL base, weaker anomalies in the AW core, and a weakened thermocline stratification. Figures 7b and 7c show that these observed anomalies in the Lomonosov Ridge region are better reproduced by the model when the coupling term is taken into account: the salinity anomaly deepens to 90 m, and the negative stratification anomaly is also shifted downward by approximately 40 m, leading to an even more reduced stratification in the thermocline (100–200 m). In the absence of the coupling term, salinity and stratification anomaly maxima are weaker by the end of the simulation. The model also reproduces the stronger temperature anomalies in the thermocline compared to the AW core in the Lomonosov Ridge region (Figure 7a), but presents a warm bias over the whole water column. This could be the result of the too simplistic representation of surface processes leading to underestimated heat loss to the surface.

The results of the idealized simulations detail the role of the coupling term to accumulate temperature and salinity anomalies at the CHL base under certain conditions. In all simulations, when maintaining a fixed background stratification (simulations 2bis, 3bis, 4bis, and 5bis), both maximum temperature, salinity and stratification anomalies are attenuated and spread vertically by the end of the simulations. On the contrary, when the coupling between stratification anomalies and diffusive fluxes is accounted for, larger temperature and salinity anomalies are obtained at the CHL base (around 100 m) at the end of the simulations, except in simulations 5/5bis.

The coupled term reads $\Gamma \frac{\partial}{\partial z}\left(\frac{\varepsilon N^{2\prime}}{N^4_{\mathrm{ref}}}\frac{\partial T_{\mathrm{ref}}}{\partial z}\right)$ in the temperature equation (Equation 6). In simulations 2, 3, and 4 with a negative stratification anomaly in the thermocline ($N^{2\prime} < 0$), $\frac{\varepsilon N^{2\prime}}{N^4_{\mathrm{ref}}}$ is negative between the CHL base and the AW core but near zero or positive in the CHL, reflecting a strong vertical stratification anomaly gradient (Figures 7i and 7l). This leads to the accumulation of T-S anomalies at the CHL base. This is particularly visible in simulations 3 and 4, where the salinity anomaly is amplified by the end of the simulations (Figures 7h and 7k), leading to an even stronger stratification weakening in the thermocline (Figures 7i and 7l). The initial negative stratification anomaly in the thermocline is present when initial positive temperature and salinity anomalies are colocated, because the density is primarily salinity-driven close to the surface (and therefore saltier waters are denser) and temperature-driven in the AW core (warmer waters are less dense). Having an initial salinity anomaly above the initial temperature anomaly (simulation 3, Figures 7g–7i)—like in the observations—leads to an even stronger stratification weakening as both temperature and salinity anomalies have a destratifying effect in the thermocline.

In simulations 3 and 4, where initial T-S anomalies are closer to the AW core, the reduced thermocline stratification leads to an upward displacement of the anomaly maxima, from 200 m at the start of the simulations, to

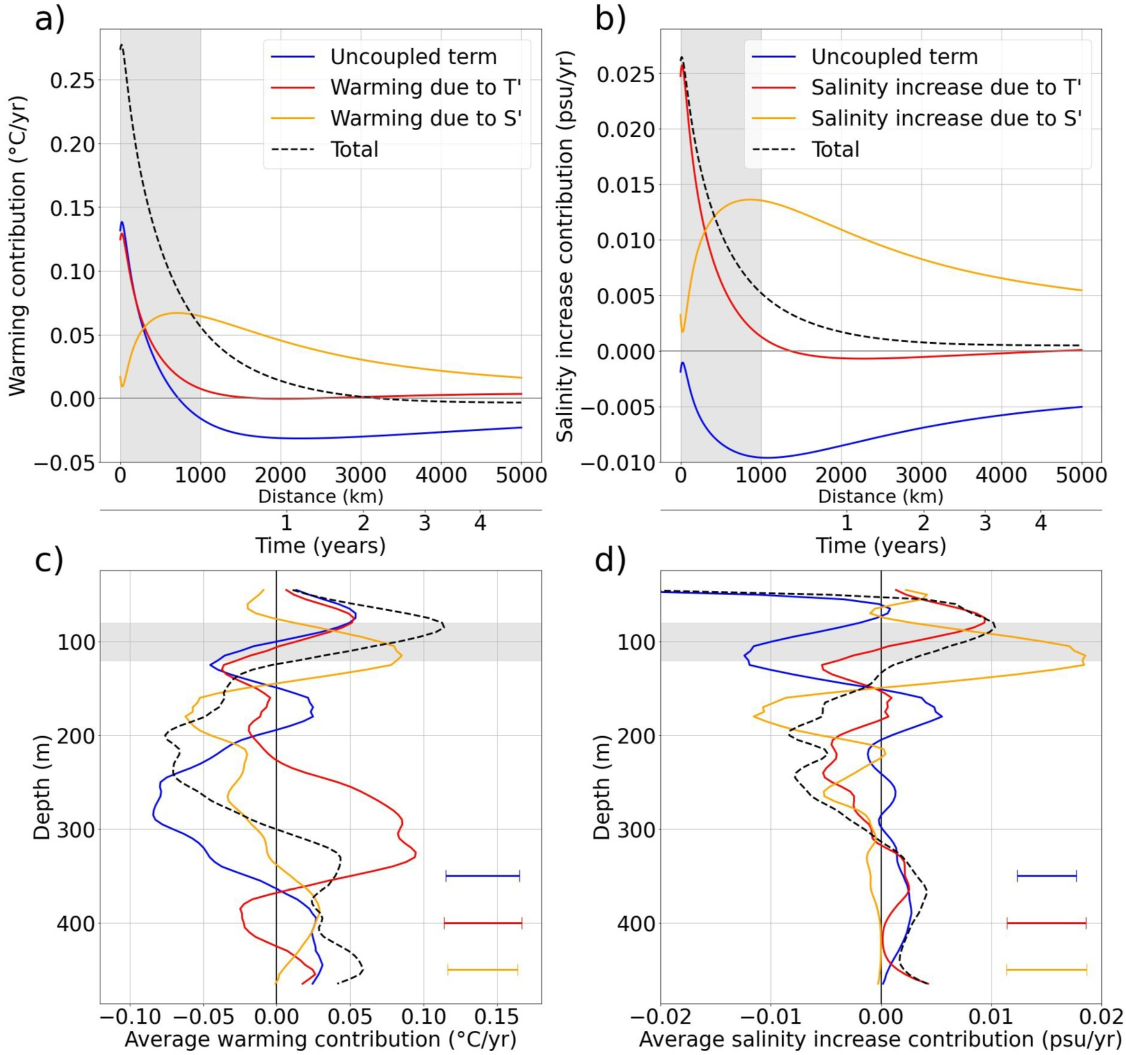

Figure 9. Vertically-averaged contributions of the different terms of Equation 6 to the diffusion of the (a) temperature and (b) salinity anomalies between 80 and 120 m (shaded areas in (c, d)) in simulation 3. Time averages over the first months of simulation (shaded areas in (a, b)) of the different contributions to the (c) temperature and (d) salinity anomalies as a function of depth in simulation 3. The profiles in (c) and (d) are smoothed vertically with a 50 m interval running mean.

130 m at the end (Figures 7g, 7j, and 7k). This is caused by the presence of strong vertical gradients in the reference state in the thermocline—$\left(\frac{\partial T_{\mathrm{ref}}}{\partial z}\right)$ and $\left(\frac{\partial S_{\mathrm{ref}}}{\partial z}\right)$—which strengthen the contribution of the coupled term in Equation 6. This implies that the coupled term preferentially accumulates anomalies at depths of largest vertical temperature and salinity gradients. In simulations 2, 3, and 4, the coupled term also induces warmer anomalies between 300 and 400 m (Figures 7d, 7g, and 7j), in the temperature gradient below the AW core, meaning that the AW core has thickened by the end of the simulations.

Conversely, in simulations 5/5bis, the initial temperature anomaly maximum is above the initial salinity anomaly maximum. This induces a positive stratification anomaly in the thermocline (Figure 7o). The coupled term then leads to weaker T-S anomalies at the CHL base by the end of the simulations (Figures 7m and 7n). Figure 8 further illustrates the contrast between the accumulation of T-S anomalies at the CHL base in simulation 3 (Figures 8a and 8b), and the vertical spreading of the T-S anomalies in simulation 5 (Figures 8d and 8e), associated with opposite stratification anomalies between the two simulations (Figures 8c and 8f).

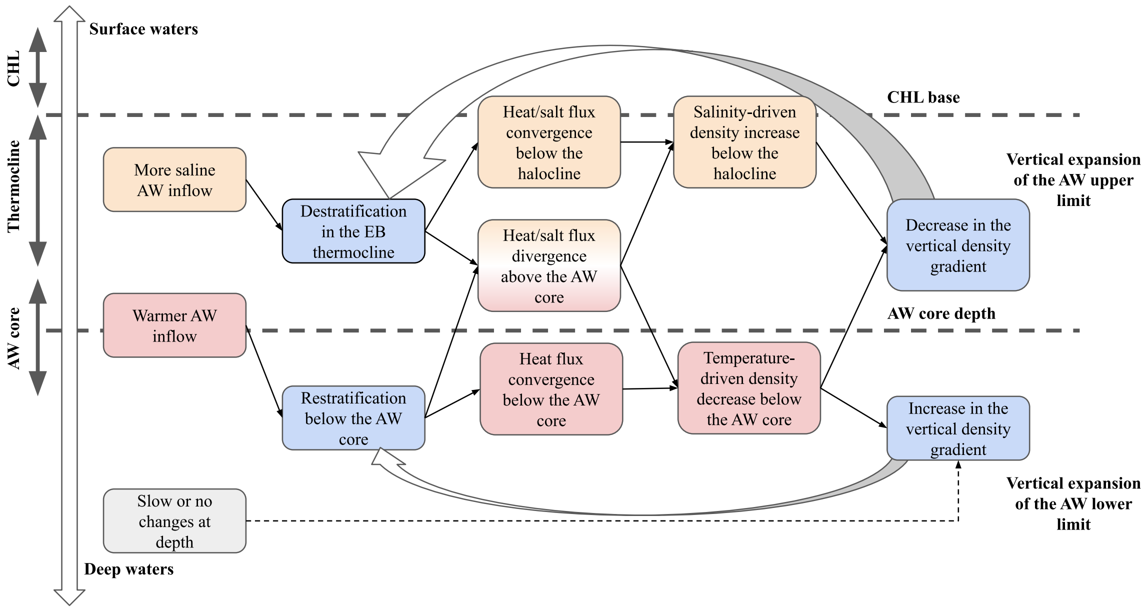

Figure 10. Summary of the processes contributing to the thickening of the Atlantic Water layer in the conceptual model.

4.3. Role of the Coupled Term on the Vertical Diffusion of Anomalies

Figures 9a and 9b show the relative contributions of the different diffusion terms affecting temperature and salinity anomaly changes between 80 and 120 m (around the CHL base in Figure 7) in simulation 3. The “coupled term” is split between the temperature and salinity contributions to the stratification changes. Both contributions (red and orange curves in Figures 9a and 9b) tend to increase temperature and salinity anomalies at the CHL base throughout the simulation, with the salinity contribution to this coupled term primarily responsible for maintaining these anomalies beyond a distance of 1,000 km from the source region. The “uncoupled term” has an opposite effect on salinity anomalies during the whole simulation, and on temperature anomalies during the last 4,000 km. By the end of the simulations, these three terms nearly balance. Figures 9c and 9d display the time-averaged contributions of these terms as a function of depth during the first few months of simulation 3, highlighting how the coupling transfers both heat and salt from the upper part of the AW layer (150–250 m) to the base of the CHL (80–120 m). Meanwhile, the temperature contribution significantly affects the warming distribution below the AW core (around 300 m at the start of the simulations). At this depth, salinity anomalies are relatively weak (Figure 7h), while temperature anomalies feature a vertical gradient between the warming AW core and weaker changes further down (Figure 7g), which has a restratifying effect (Figure 7i). Similarly to the temperature and salinity anomalies trapped between the layer of reduced stratification and the CHL around 100 m, temperature anomalies below the AW core are trapped above the layer of increased stratification. In simulation 3, this leads to the emergence of a second temperature anomaly maximum below the AW core (Figure 7g). Combined together, these processes result in a thickening of the AW core—both upwards and downwards -, as summarized in Figure 10.

5. Discussion and Conclusion

We clustered WOD hydrographic data into regions defined by consistent vertical structure of the *T-S* properties. Identifying trends and variability for each region separately revealed two distinct variability regimes: significant multi-decadal warming and salinification trends in the thermocline in the Eurasian Basin interior and anomalies lasting for several years at the basin periphery (mainly in the AW boundary current and over the Lomonosov Ridge). The timing of these anomalies is found to be consistent with an origin in the successive warm anomalies which have been observed in the AW layer in Fram Strait and the Eurasian Basin (Beszczynska-Möller et al., 2012; Morison et al., 1998; Quadfasel et al., 1991), suggesting an advective component in the reconstructed anomalies. In the basin interior, the absence of such anomalies may reflect the diffusion of properties by eddies through shelf-basin exchanges, which are known to take place at various locations around the basin (Crews et al., 2018).

An important result of our analysis is that the identified anomalies and trends are associated with a reduced stratification in a layer which can extend from the CHL base to a depth beyond the AW core, concomitantly to a stratification increase in the lower part of the AW layer. The weakening stratification over the 35-year study period is clearly detected in the continuous upward and downward displacements of the $\sigma = 27.8$ kg m^{-3} and $\sigma = 27.93$ kg m^{-3} isopycnals defining the upper and lower boundary of the AW core layer, respectively. This evolution traces the vertical spreading of a progressively thicker, less stratified AW layer, consistent with earlier results highlighting an upward displacement of the AW upper boundary during the recent decades (Polyakov et al., 2010, 2017), and extending these results to the downward expansion of the AW core lower boundary. At the AW core depth, no significant evidence of a temperature change was found. Other recent studies investigating changes in AW core temperature since the 1990s have led to contradictory results: Polyakov et al. (2012) found a warming between the 1990s and the 2000s, while Kong et al. (2025) suggest a cooling occurred over the same period. This contradiction likely stems from the different data processing used in these studies: in particular, Kong et al. (2025) do not take into account the changes in the geographical distribution of available data over the past 35 years.

Building on the hypothesis that warm and saline anomalies encountered in the Eurasian Basin have an advective component and that their origin can be found in the properties of the AW inflow entering the basin through Fram Strait, we used a simple advective-diffusive model to evaluate the role of advection and diffusion in shaping the vertical structure of the anomalies and their time evolution. Prescribing initial anomalies similar to those observed at the basin entrance, we showed that this conceptual model could reproduce the general structure of salinity and stratification anomalies further in the basin. Performing additional idealized simulations, we showed that the changes in stratification driven by *T-S* anomalies were necessary to account for the observed accumulation of these anomalies in the thermocline. This coupling tends to accumulate anomalies in layers of strong vertical temperature and salinity gradients when a vertical stratification anomaly gradient is present (with a weaker stratification anomaly at greater depths).

The results were found to be insensitive to longer advection times and minor variations of the boundary conditions. The main reason for this insensitivity to advection times seems to be that the timescale associated with the coupling term $-\Gamma \frac{\partial}{\partial z}\left(\frac{\varepsilon N'^2}{N_{\mathrm{ref}}^4}\frac{\partial T_{\mathrm{ref}}}{\partial z}\right)$ is close to a year and is thus shorter than realistic advection timescales around the basin (at least 5 years). In the CHL, model results are less robust and probably less reliable. The model has a simplistic representation of the surface layer. Dampening of surface temperature anomalies allows anomalous heat loss to the atmosphere, even if it does not capture the seasonality of the CHL stratification. One might wonder whether anomalous surface heat loss in winter could release the entire advected heat content. But the persistence of warm anomalies below the CHL in our data suggests that such heat loss would not be sufficient and anomalies would still persist.

5.1. Outlook

The model was initially designed to understand the response of a water column to short-lived anomalies entering the basin, and it is not obvious whether the coupling between reduced AW stratification and AW thickening could play a role in the AW long-term trends found in the WOD data. Trends in the Eurasian Basin's *T-S* properties are the result of diverse influences, including changes in surface heat and freshwater fluxes, which may dominate over changes in vertical diffusion caused by increasingly warm and more weakly stratified AW inflows. Still, trends in the WOD data (Figure 4), in particular in the Eurasian Basin's interior, show a very similar vertical structure compared to the anomalies obtained at the end of the simulations at the arrival of a warm and saline anomaly (Figure 7). This suggests that the weakening of stratification in the thermocline may be of importance to explain the AW thickening trend there. Although they may be important locally, the other processes may be sporadic enough to be filtered out over the long term and allow vertical diffusion to emerge as the dominant driver of changes in the AW layer.

In previous studies, the observed weakening stratification trend in the Eurasian Basin was mostly envisaged as being triggered, at least partly, by the advection of salinity anomalies forming at the ice edge, in particular in the Barents Sea (Polyakov et al., 2020). In this article, we proposed a new cause for the weakening of stratification in the Eurasian Basin, which originates in the variability of AW properties in Fram Strait, and introduced a diffusion mechanism linking the structure of anomalies at the basin entrance and along their pathway. This weakening of stratification is expected to have significant implications for vertical heat fluxes up to the base of the CHL. However, it remains unclear whether this heat will ultimately be transferred to the sea ice. Using mooring data from the eastern Eurasian, Makarov, and Canada Basins, Polyakov et al. (2025) recently observed enhanced wintertime heat fluxes to the surface as far east as the Makarov Basin, but not in the more strongly stratified Canada Basin. Given the stratification differences among the various subdomains of the Eurasian Basin, further studies focusing on surface processes are needed to assess the impact of AW thickening on the sea-ice cover at basin scale.

Conflict of Interest

The authors declare no conflicts of interest relevant to this study.

Data Availability Statement

The WOD data can be found in Boyer et al. (2018). The WOA climatology can be accessed on the website: https://www.nodc.noaa.gov/OC5/woa18/. CTD data from the MOSAiC expedition can be downloaded from the PANGAEA database (Tippenhauer et al., 2023). CTD casts from the NABOS 2018 and 2021 campaigns are available on the NABOS website: https://uaf-iarc.org/nabos.

Acknowledgments
The work presented in this article was supported by the Agence de l'Innovation de Défense via the funding contract AID 2023 65 0067. The work presented in this article was supported by the AMOSA project as part of the LEFE programme.

References

Aagaard, K. (1989). A synthesis of the Arctic Ocean circulation. Rapports et procès-verbaux des réunions (1903–1991). Report. https://doi.org/10.17895/ices.pub.19279133.v1

Athanase, M., Provost, C., Pérez-Hernández, M. D., Sennéchael, N., Bertosio, C., Artana, C., et al. (2020). Atlantic water modification north of Svalbard in the Mercator physical system from 2007 to 2020. *Journal of Geophysical Research: Oceans*, *125*(10), e2020JC016463. https://doi.org/10.1029/2020JC016463

Baumann, T. M., Polyakov, I. V., Pnyushkov, A. V., Rember, R., Ivanov, V. V., Alkire, M. B., et al. (2018). On the seasonal cycles observed at the Continental slope of the Eastern Eurasian Basin of the Arctic Ocean. *Journal of Physical Oceanography*, *48*(7), 1451–1470. https://doi.org/10.1175/JPO-D-17-0163.1

Beszczynska-Möller, A., Fahrbach, E., Schauer, U., & Hansen, E. (2012). Variability in Atlantic water temperature and transport at the entrance to the Arctic Ocean, 1997–2010. *ICES Journal of Marine Science*, *69*(Issue 5), 852–863. https://doi.org/10.1093/icesjms/fss056

Boyer, T. P., Baranova, O. K., Coleman, C., Garcia, H. E., Grodsky, A., Locarnini, R. A., et al. (2018). World Ocean Database 2018 [Dataset]. *A. V. Mishonov (Ed.), NOAA Atlas NESDIS 87*. https://www.ncei.noaa.gov/products/world-ocean-database

Carmack, E., Polyakov, I., Padman, L., Fer, I., Hunke, E., Hutchings, J., et al. (2015). Toward quantifying the increasing role of Oceanic heat in Sea ice loss in the new Arctic. *Bulletin America Meteorology Social*, *96*(12), 2079–2105. https://doi.org/10.1175/BAMS-D-13-00177.1

Challet, F., Geyer, F., Bertino, L., & Raj, R. P. (2022). Oceanography of the Fram Strait—Improving general understanding and models through the use of mooring interpolation products. *Zenodo*. https://doi.org/10.5281/zenodo.7377340

Charette, M. A., Kipp, L. E., Jensen, L. T., Dabrowski, J. S., Whitmore, L. M., Fitzsimmons, J. N., et al. (2020). The Transpolar Drift as a source of riverine and shelf-derived trace elements to the central Arctic Ocean. *Journal of Geophysical Research: Oceans*, *125*(5), e2019JC015920. https://doi.org/10.1029/2019JC015920

Crews, L., Sundfjord, A., Albretsen, J., & Hattermann, T. (2018). Mesoscale eddy activity and transport in the Atlantic Water inflow region north of Svalbard. *Journal of Geophysical Research: Oceans*, *123*(1), 201–215. https://doi.org/10.1002/2017JC013198

Fer, I., Peterson, A. K., Randelhoff, A., & Meyer, A. (2017). One-dimensional evolution of the upper water column in the Atlantic sector of the Arctic Ocean in winter. *Journal of Geophysical Research: Oceans*, *122*(3), 1665–1682. https://doi.org/10.1002/2016JC012431

Hartigan, J. A., & Wong, M. A. (1979). Algorithm AS 136: A K-Means Clustering Algorithm. *Journal of the Royal Statistical Society. Series C (Applied Statistics)*, *28*(1), 100–108. https://doi.org/10.2307/2346830

Holliday, N. P., Cunningham, S. A., Johnson, C., Gary, S. F., Griffiths, C., Read, J. F., & Sherwin, T. (2015). Multidecadal variability of potential temperature, salinity, and transport in the eastern subpolar North Atlantic. *Journal of Geophysical Research: Oceans*, *120*(9), 5945–5967. https://doi.org/10.1002/2015JC010762

Isachsen, P., Lacasce, J., Mauritzen, C., & Häkkinen, S. (2003). Wind-Driven variability of the large-scale recirculating flow in the nordic Seas and Arctic Ocean. *Journal of Physical Oceanography*, *33*, 2534. https://doi.org/10.1175/1520-0485

Karcher, M., Kauker, F., Gerdes, R., Hunke, E., & Zhang, J. (2007). On the dynamics of Atlantic Water circulation in the Arctic Ocean. *Journal of Geophysical Research*, *112*(C4), C04S02. https://doi.org/10.1029/2006JC003630

Kong, B., Gao, L., Wang, S., & Guo, G. (2025). Cooling and sinking of the Atlantic water in the Eurasian Basin since 1990s. *Geophysical Research Letters*, *52*(9), e2025GL114720. https://doi.org/10.1029/2025GL114720

Lenn, Y., Rippeth, T. P., Old, C. P., Bacon, S., Polyakov, I., Ivanov, V., & Hölemann, J. (2011). Intermittent intense turbulent mixing under ice in the laptev Sea Continental Shelf. *Journal of Physical Oceanography*, *41*(3), 531–547. https://doi.org/10.1175/2010JPO4425.1

Locarnini, R. A., Mishonov, A. V., Antonov, J. I., Boyer, T. P., Garcia, H. E., Baranova, O. K., et al. (2013). Temperature. Vol. 1, World Ocean Atlas 2013, NOAA Atlas NESDIS 73 (p. 40). Retrieved from https://data.nodc.noaa.gov/woa/WOA13/DOC/woa13_vol1.pdf

Metzner, E. P., & Salzmann, M. (2023). Technical note: Determining Arctic Ocean halocline and cold halostad depths based on vertical stability. *Ocean Science*, *19*(5), 1453–1464. https://doi.org/10.5194/os-19-1453-2023

Meyer, A., Fer, I., Sundfjord, A., & Peterson, A. K. (2017). Mixing rates and vertical heat fluxes north of Svalbard from Arctic winter to spring. *Journal of Geophysical Research: Oceans*, *122*(6), 4569–4586. https://doi.org/10.1002/2016JC012441

Morison, J., Kwok, R., Peralta-Ferriz, C., Alkire, M., Rigor, I., Andersen, R., & Steele, M. (2012). Changing Arctic Ocean freshwater pathways. *Nature*, *481*(7379), 66–70. https://doi.org/10.1038/nature10705

Morison, J., Steele, M., & Andersen, R. (1998). Hydrography of the upper Arctic Ocean measured from the nuclear submarine U.S.S. Pargo. *Deep Sea Research Part I: Oceanographic Research Papers*, *45*(1), 15–38. https://doi.org/10.1016/S0967-0637(97)00025-3

Muilwijk, M., Nummelin, A., Heuzé, C., Polyakov, I. V., Zanowski, H., & Smedsrud, L. H. (2023). Divergence in climate model projections of future Arctic atlantification. *Journal of Climate*, *36*, 1727–1748. https://doi.org/10.1175/JCLI-D-22-0349.1

Osborn, T. R. (1980). Estimates of the local rate of vertical diffusion from dissipation measurements. *Journal of Physical Oceanography*, *10*, 83–89. https://doi.org/10.1175/1520-0485(1980)010<0083:EOTLRO>2.0.CO;2

Pérez-Hernández, M. D., Pickart, R. S., Pavlov, V., Våge, K., Ingvaldsen, R., Sundfjord, A., et al. (2017). The Atlantic Water boundary current north of Svalbard in late summer. *Journal of Geophysical Research: Oceans*, *122*(3), 2269–2290. https://doi.org/10.1002/2016JC012486

Polyakov, I. V., Alekseev, G. V., Timokhov, L. A., Bhatt, U. S., Colony, R. L., Simmons, H. L., et al. (2004). Variability of the intermediate Atlantic water of the Arctic Ocean over the last 100 years. *Journal of Climate*, *17*(23), 4485–4497. https://doi.org/10.1175/jcli-3224.1

Polyakov, I. V., Alexeev, V. A., Belchansky, G. I., Dmitrenko, I. A., Ivanov, V. V., Kirillov, S. A., et al. (2008). Arctic Ocean freshwater changes over the past 100 years and their causes. *Journal of Climate*, *21*(2), 364–384. https://doi.org/10.1175/2007JCLI1748.1

Polyakov, I. V., Beszczynska, A., Carmack, E. C., Dmitrenko, I. A., Fahrbach, E., Frolov, I. E., et al. (2005). One more step toward a warmer Arctic. *Geophysical Research Letters*, *32*(17), L17605. https://doi.org/10.1029/2005GL023740

Polyakov, I. V., Ingvaldsen, R. B., Pnyushkov, A. V., Bhatt, U. S., Francis, J. A., Janout, M., et al. (2023). Fluctuating Atlantic inflows modulate Arctic atlantification. *Science*, *381*(6661), 972–979. https://doi.org/10.1126/science.adh5158

Polyakov, I. V., Pnyushkov, A. V., Alkire, M. B., Ashik, I. M., Baumann, T. M., Carmack, E. C., et al. (2017). Greater role for Atlantic inflows on sea-ice loss in the Eurasian Basin of the Arctic Ocean. *Science*, *356*(6335), 285–291. https://doi.org/10.1126/science.aai8204

Polyakov, I. V., Pnyushkov, A. V., Charette, M., Cho, K. H., Jung, J., Kipp, L., et al. (2025). Atlantification advances into the Amerasian Basin of the Arctic Ocean. *Science Advances*, *11*(8), eadq7580. https://doi.org/10.1126/sciadv.adq7580

Polyakov, I. V., Pnyushkov, A. V., & Timokhov, L. A. (2012). Warming of the intermediate Atlantic water of the Arctic Ocean in the 2000s. *Journal of Climate*, *25*(23), 8362–8370. https://doi.org/10.1175/JCLI-D-12-00266.1

Polyakov, I. V., Rippeth, T. P., Fer, I., Alkire, M. B., Baumann, T. M., Carmack, E. C., et al. (2020). Weakening of cold halocline layer exposes sea ice to oceanic heat in the Eastern Arctic Ocean. *Journal of Climate*, *33*(18), 8107–8123. https://doi.org/10.1175/JCLI-D-19-0976.1

Polyakov, I. V., Timokhov, L. A., Alexeev, V. A., Bacon, S., Dmitrenko, I. A., Fortier, L., et al. (2010). Arctic Ocean warming contributes to reduced polar ice cap. *Journal of Physical Oceanography*, *40*(12), 2743–2756. https://doi.org/10.1175/2010JPO4339.1

Quadfasel, D., Sy, A., Wells, D., & Tunik, A. (1991). Warming in the Arctic. *Nature*, *350*(6317), 385. https://doi.org/10.1038/350385a0

Rabe, B., Heuzé, C., Regnery, J., Aksenov, Y., Allerholt, J., Athanase, M., et al. (2022). Overview of the MOSAiC expedition: Physical oceanography. *Elementa: Science of the Anthropocene*, *10*(1), 00062. https://doi.org/10.1525/elementa.2021.00062

Rantanen, M., Karpechko, A. Y., Lipponen, A., Nordling, K., Hyvärinen, O., Ruosteenoja, K., et al. (2022). The Arctic has warmed nearly four times faster than the globe since 1979. *Communications Earth & Environment*, *3*(1), 168. https://doi.org/10.1038/s43247-022-00498-3

Richards, A. E., Johnson, H. L., & Lique, C. (2022). Spatial and temporal variability of Atlantic Water in the Arctic from 40 years of observations. *Journal of Geophysical Research: Oceans*, *127*(9), e2021JC018358. https://doi.org/10.1029/2021JC018358

Rosenblum, E., Stroeve, J., Gille, S. T., Lique, C., Fajber, R., Tremblay, L. B., et al. (2022). Freshwater input and vertical mixing in the Canada basin's seasonal halocline: 1975 versus 2006–12. *Journal of Physical Oceanography*, *52*(7), 1383–1396. https://doi.org/10.1175/JPO-D-21-0116.1

Ruiz-Castillo, E., Janout, M., Hölemann, J., Kanzow, T., Schulz, K., & Ivanov, V. (2023). Structure and seasonal variability of the Arctic Boundary Current north of Severnaya Zemlya. *Journal of Geophysical Research: Oceans*, *128*(1), e2022JC018677. https://doi.org/10.1029/2022JC018677

Santer, B. D., Wigley, T. M. L., Boyle, J. S., Gaffen, D. J., Hnilo, J. J., Nychka, D., et al. (2000). Statistical significance of trends and trend differences in layer-average atmospheric temperature time series. *Journal of Geophysical Research*, *105*(D6), 7337–7356. https://doi.org/10.1029/1999JD901105

Schauer, U., Fahrbach, E., Osterhus, S., & Rohardt, G. (2004). Arctic warming through the Fram Strait: Oceanic heat transport from 3 years of measurements. *Journal of Geophysical Research*, *109*(C6), C06026. https://doi.org/10.1029/2003JC001823

Schulz, K., Lincoln, B., Povazhnyy, V., Rippeth, T., Lenn, Y.-D., Janout, M., et al. (2022). Increasing nutrient fluxes and mixing regime changes in the eastern Arctic Ocean. *Geophysical Research Letters*, *49*(5), e2021GL096152. https://doi.org/10.1029/2021GL096152

Storch, H. V. (1998). Statistical analysis in climate research/Hans von Storch and Francis W. Zwiers. P. cm. Includes index. In *Climatology—Statistical methods. I* (pp. 151–152). CIP.

Sundfjord, A., Lundesgaard, Ø., & Renner, A. H. (2022). A-TWAIN mooring data 2019–2020 [Dataset]. *Norwegian Polar Institute*. https://doi.org/10.21334/NPOLAR.2022.D3A5ADC2

Swift, J. H., Jones, E. P., Aagaard, K., Carmack, E. C., Hingston, M., MacDonald, R. W., et al. (1997). Waters of the Makarov and Canada basins. *Deep Sea Research Part II: Topical Studies in Oceanography*, *44*(8), 1503–1529. https://doi.org/10.1016/S0967-0645(97)00055-6

Tippenhauer, S., Vredenborg, M., Heuzé, C., Ulfsbo, A., Rabe, B., Granskog, M. A., et al. (2023). Physical oceanography water bottle samples based on ship CTD during POLARSTERN cruise PS122, physical oceanography based on ship CTD during POLARSTERN cruise PS122, physical oceanography water bottle samples based on Ocean City CTD during POLARSTERN cruise PS122, physical oceanography based on Ocean City CTD during POLARSTERN cruise PS122 [Dataset]. *PANGAEA*. https://doi.org/10.1594/PANGAEA.959965

Våge, K., Pickart, R. S., Pavlov, V., Lin, P., Torres, D. J., Ingvaldsen, R., et al. (2016). The Atlantic Water boundary current in the Nansen Basin: Transport and mechanisms of lateral exchange. *Journal of Geophysical Research: Oceans*, *121*(9), 6946–6960. https://doi.org/10.1002/2016JC011715

Zweng, M. M., Reagan, J. R., Seidov, D., Boyer, T. P., Locarnini, R. A., Garcia, H. E., et al. (2019). World Ocean Atlas 2018, volume 2: Salinity. In A. Mishonov (Ed.), *NOAA Atlas NESDIS* (Vol. 82, p. 50).